



Heterogeneous and rate-dependent streptavidin–biotin unbinding revealed by high-speed force spectroscopy and atomistic simulations

Felix Rico^{a,1,2}, Andreas Russek^{b,1}, Laura González^c, Helmut Grubmüller^{b,2}, and Simon Scheuring^{d,e,2}

^aLaboratoire Adhésion et Inflammation (LAI), Aix-Marseille Université, CNRS, INSERM, 13009 Marseille, France; ^bDepartment of Theoretical and Computational Biophysics, Max Planck Institute for Biophysical Chemistry, 37077 Göttingen, Germany; ^cDepartment of Electronics, Universitat de Barcelona, 08028 Barcelona, Spain; ^dDepartment of Anesthesiology, Weill Cornell Medical College, New York, NY 10065; and ^eDepartment of Physiology and Biophysics, Weill Cornell Medical College, New York, NY 10065

Edited by Taekjip Ha, Johns Hopkins University, Baltimore, MD, and approved February 21, 2019 (received for review October 4, 2018)

Receptor–ligand interactions are essential for biological function and their binding strength is commonly explained in terms of static lock-and-key models based on molecular complementarity. However, detailed information on the full unbinding pathway is often lacking due, in part, to the static nature of atomic structures and ensemble averaging inherent to bulk biophysics approaches. Here we combine molecular dynamics and high-speed force spectroscopy on the streptavidin–biotin complex to determine the binding strength and unbinding pathways over the widest dynamic range. Experiment and simulation show excellent agreement at overlapping velocities and provided evidence of the unbinding mechanisms. During unbinding, biotin crosses multiple energy barriers and visits various intermediate states far from the binding pocket, while streptavidin undergoes transient induced fits, all varying with loading rate. This multistate process slows down the transition to the unbound state and favors rebinding, thus explaining the long lifetime of the complex. We provide an atomistic, dynamic picture of the unbinding process, replacing a simple two-state picture with one that involves many routes to the lock and rate-dependent induced-fit motions for intermediates, which might be relevant for other receptor–ligand bonds.

high-speed atomic force microscopy | high-speed force spectroscopy | receptor/ligand bonds | single molecules | molecular dynamics simulations

Receptor/ligand bonds are at the core of almost every biological process. The early lock-and-key model including possible conformational changes of the binding partners is commonly accepted to describe the affinities and kinetic rates of receptor/ligand complexes and is mainly based on molecular complementarity pictures from static structural data (1, 2). Over the past decades, an impressive amount of knowledge has been accumulated on the structural and energetic determinants of bound states, thus enabling the increasingly successful rational design of nanomolar binders for therapy as well as the quantitative prediction of binding processes and free energies from atomistic simulations (3). While protein folding and unfolding are thought to follow a multiplicity of pathways, the very mechanism of binding or unbinding of receptor/ligand complexes remains less investigated and is generally described by a simple two-state model, or by the lock-and-key analogy. Moreover, little is known on how the (un)binding dynamics is governed by the underlying microscopic processes—despite being key to a quantitative understanding of receptor–ligand complexes. Progress is mostly hampered by the lack of structural and thermodynamic information of the transient ligand/receptor conformations during unbinding, even for extensively studied systems such the complex formed by streptavidin (SA) and the small molecule biotin (b, vitamin H), one of the strongest noncovalent bonds known in nature.

SA forms the b-binding pocket with an eight-stranded, antiparallel beta-barrel capped by loop 3–4 (Fig. 1A). In the native, tetrameric SA form, loop 7–8 from an adjacent monomer provides

a closing lid to the pocket (4). b binds by forming an intricate and extensive network of hydrogen bonds with polar residues of SA (4, 5). Its high affinity ($K_d \sim 10^{-13}$ M) and long lifetime ($\tau \sim 10$ d, $k_{\text{off}} \sim 10^{-6}$ s⁻¹) (6–9) make the SA/b system extensively used in biotechnology and biophysics. Dynamic forced disruption of the SA–b complex by atomic force microscopy (AFM) and other techniques pioneered single-molecule biomechanics (10–13) and provided estimates of the distance x_β to the unbinding transition state and the intrinsic bond lifetime (13–15). Despite its seeming simplicity, AFM (11, 16–19), optical tweezers (20), and biomembrane force probe (10, 21) experiments of SA/b unbinding have reported dissimilar results, suggesting an impressive complexity and heterogeneity in the unbinding pathway (*SI Appendix*). Furthermore, the results from single-molecule studies were incompatible with ensemble bond-lifetime measurements (6).

Although recent experimental developments accessing the microsecond timescale have shed light into the complexity of single-molecule transition paths of protein and nucleic acid (un) folding (22–25), the amount of transient structural information extracted from single-molecule experiments is rather limited.

Significance

Protein–ligand interactions are commonly described in terms of a two-state or a lock-and-key mechanism. To provide a more detailed and dynamic description of receptor–ligand bonds and their (un)binding path, we combined high-speed force spectroscopy and molecular dynamics simulations to probe the prototypical streptavidin–biotin complex. The excellent agreement observed, never used for force-field refinement, provides the most direct test of the “computational microscope.” The so far largest dynamic range of loading rates explored (11 decades) enabled accurate reconstruction of the free-energy landscape. We revealed velocity-dependent unbinding pathways and intermediate states that enhance rebinding, explaining the long lifetime of the bond. We expect similar behavior in most receptor–ligand complexes, implying unbinding pathways governed by transient, timescale-dependent induced fits.

Author contributions: F.R., A.R., L.G., H.G., and S.S. designed research; F.R., A.R., L.G., and H.G. performed research; F.R., A.R., and H.G. analyzed data; and F.R., A.R., H.G., and S.S. wrote the paper.

The authors declare no conflict of interest.

This article is a PNAS Direct Submission.

This open access article is distributed under [Creative Commons Attribution-NonCommercial-NoDerivatives License 4.0 \(CC BY-NC-ND\)](https://creativecommons.org/licenses/by-nc-nd/4.0/).

¹F.R. and A.R. contributed equally to this work.

²To whom correspondence may be addressed. Email: felix.rico@inserm.fr, hgrubmu@gwdg.de, or sis2019@med.cornell.edu.

This article contains supporting information online at www.pnas.org/lookup/suppl/doi:10.1073/pnas.1816909116/-DCSupplemental.

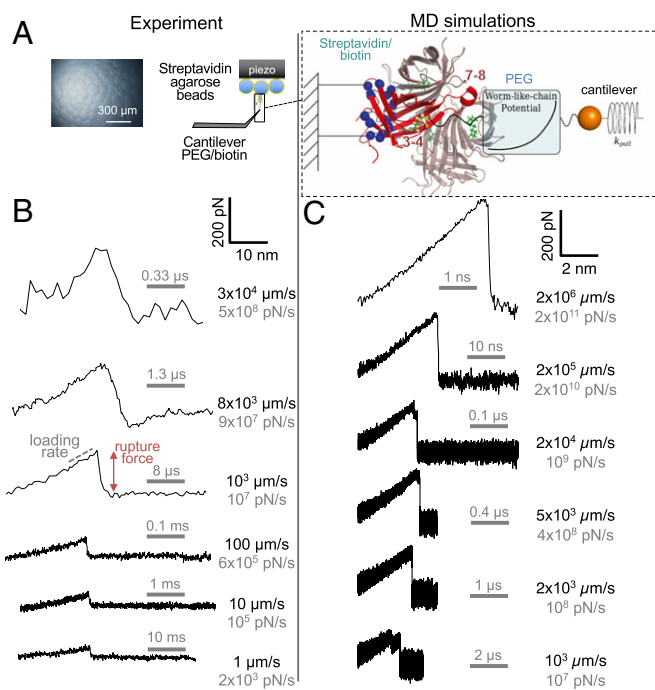


Fig. 1. High-speed and MD force spectroscopy of SA–b unbinding. (A, Left) HS-FS setup. SA agarose beads (Top Left) were immobilized on the sample surface while b was covalently attached to the microcantilever (Bottom Left) through a PEG linker (contour length ~ 10 nm). (A, Right) MD simulations setup and the SA–b tetramer used in the MD simulations with labeled loops 3–4 and 7–8 (PDB ID code 3RY2). (B) Experimental force–distance traces at velocities from $1 \mu\text{m/s}$ to $30,556 \mu\text{m/s}$ revealing bond rupture events using AC7 (top curve) and AC10 cantilevers (bottom curves). The stretching profile of the experimental curves was the result of stretching the PEG linker and deforming the agarose bead to which SA was linked. (C) Force–extension traces from the MD simulations at retraction velocities from $1,000 \mu\text{m/s}$ to $2 \times 10^6 \mu\text{m/s}$.

Therefore, most structural knowledge on unbinding/unfolding processes has been derived from atomistic simulations that were often limited to short timescales inaccessible to experiments and therefore not rigorously validated (24–28). Thus, today, a direct relationship between the energy landscape and the dynamic structural details of these seemingly simple biomolecular processes is missing. As a result, it is still unclear (i) how b precisely outlives days and unbinds under load, (ii) how and where b is located at the point of rupture and how the respective intermediates are stabilized, (iii) if there is only one or possibly several unbinding pathways, and if so, (iv) to what extent the unbinding paths change with loading rate. Here we address these questions by combining high-speed force spectroscopy (HS-FS) and fully atomistic simulations to observe b unbinding from SA over 11 decades of loading rates. We show that the unbinding pathway of the small molecule b from SA is much more complex than a “key that leaves a lock” and reveal a multitude of pathways and intermediate binding sites far from the binding pocket, similar to the various pathways and intermediate states of protein (un)folding.

For the HS-FS experiments we used microcantilevers functionalized with b to probe the force required to rupture individual SA–b bonds at various loading rates (Fig. 1A, Left). The use of microcantilevers with response time of $\sim 0.5 \mu\text{s}$ and reading out the reflected laser beam at $0.05 \mu\text{s}$ (high sampling rates up to 20 million samples per s) allowed tracking the cantilever position while pulling at velocities up to $\sim 30,000 \mu\text{m/s}$, almost an order of magnitude faster than previous HS-FS measurements and about 1,000 times faster than conventional AFM FS measurements (11, 19, 29). All atom steered molecular dynamics (SMD) simulations

precisely mimicked the experimental setup by using the fully solvated tetrameric structure of SA [Protein Data Bank (PDB) ID code 3RY2 (4)] and by pulling b using two springs in series, using the worm-like chain (WLC) model describing the PEG linker and a linear spring for the cantilever, whose end was moved at constant velocity (Fig. 1A, Right and Movies S1–S3). The overall applied pulling velocities ranged from $0.05 \mu\text{m/s}$ to $30,000 \mu\text{m/s}$ in HS-FS experiments (Fig. 1B) and from $1,000 \mu\text{m/s}$ to $5 \times 10^{10} \mu\text{m/s}$ in SMD simulations (Fig. 1C), resulting in a combined range of loading rates from ~ 100 pN/s to $\sim 10^{13}$ pN/s, covering 11 decades. Importantly, the wide experimental dynamic range up to such fast rates, together with recent simulation advances (30, 31), allowed direct overlap and comparison with in silico simulation loading rates over an entire decade between 10^8 and 10^9 pN/s (Fig. 2 and SI Appendix).

The measured force curves showed a characteristic curve of increasing force due to stretching of the flexible PEG linker (Fig. 1), signature of the specificity of the interaction (32) (Materials and Methods). Fig. 2 shows the dynamic force spectrum obtained both from the most probable rupture forces at each loading rate (in piconewtons per second) in the experiments (circles) as well as from the average rupture force of 10 to 20 simulations per loading rate (triangles). At the overlapping loading rates, rupture forces from experiments and simulations agreed very well, thereby providing independent validation for the MD simulations. At the lowest loading rates, from $\sim 10^2$ pN/s up to $\sim 10^6$ pN/s ($\sim 10^3 \mu\text{m/s}$ pulling velocity), rupture forces increased almost linearly with the logarithm of the loading rate, indicating one single dominant barrier in this loading rate regime. At faster loading rates, steeper slopes are observed. This behavior has been interpreted before in several ways: (i) multiple transition barriers along the 1D energy landscape, inner barriers becoming dominant at high loading rates and outer barriers, at low rates (10, 19); (ii) force-induced shortening of the distance to the transition state (14, 33); and (iii) a transition from a thermally activated to a so-called deterministic regime (15, 24, 34). Another possible cause (iv) might be that the cantilever response affects the force spectrum for pulling timescales shorter than the cantilever response time (35, 36). Actually, previous experiments using devices

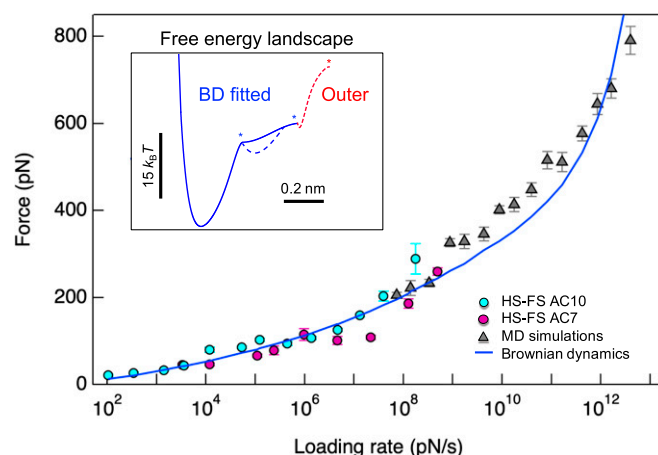


Fig. 2. Dynamic force spectrum of SA/b unbinding. Most probable rupture forces (\pm SEM) from HS-FS experiments (circles, using regular AC10 and fast AC7 cantilevers, cyan and magenta, respectively) and MD simulations (triangles). The blue line represents a Brownian dynamics fit to the whole force spectrum. (Inset) The resulting equilibrium free-energy landscape is shown as a blue line, which revealed two transition barriers (with parameters $D = 4 \times 10^7 \text{ nm}^2/\text{s}$, $\Delta G_1 = 17 k_B T$, $\Delta G_2 = 21 k_B T$, $x_{p1} = 0.19 \text{ nm}$, and $x_{p2} = 0.44 \text{ nm}$) and a possible intermediate state between the two (blue dashed line). The red dashed line sketches a third, outer barrier (Fig. 3 and text), which cannot be extracted from the dynamic force spectrum.

with a dynamic response slower than HS-FS cantilevers (response time $\tau_c \sim 50$ to $500 \mu\text{s}$, effective diffusion constant $D_p \sim 10^2$ to $10^3 \text{ nm}^2/\text{s}$, compared with $\tau_c \sim 0.5 \mu\text{s}$, $D_p \sim 10^5 \text{ nm}^2/\text{s}$) have reported a marked slope increase at loading rates $\sim 10^4$ pN/s (10, 16, 19, 29), while our first slope increase occurred at $\sim 10^6$ pN/s. This suggests that this possible effect (iv) is reduced using HS-FS microcantilevers, which allows orders of magnitude faster loading rates before this possible effect may appear.

By virtue of the broad range of loading rates covered here, the combined dynamic force spectrum contains more information on the free-energy landscape of unbinding than has been accessible before. As detailed below, all three possible explanations (i–iii) seem to contribute to the shape of the energy landscape. In particular, single-barrier models did not describe the entire dynamic force spectrum satisfactorily, supporting the presence of a more complex energy landscape with multiple barriers (14, 15, 34, 36, 37) (SI Appendix, Fig. S7). To avoid approximations inherent to analytic theories, we instead performed Brownian dynamics simulations using a more complex energy landscape with two barriers and varied the shape and height of these barriers (Fig. 2, Inset; see also SI Appendix) until the best agreement with the dynamic force spectrum (blue line in Fig. 2) was obtained. Importantly, this free-energy landscape explains both experiment and simulation over the whole 11 decades of loading rates. The energy landscape has a first (inner) $\sim 17 \text{ k}_B\text{T}$ barrier at 0.19 nm , which determines the force spectrum slope at loading rates faster than 10^6 pN/s, and a second $\sim 21 \text{ k}_B\text{T}$ unbinding barrier further out at 0.44 nm (Fig. 2, Inset, blue line). The longer rupture length of the second barrier, which becomes rate-limiting only at lower unbinding rates, gives rise to the shallower slope at loading rates below 10^6 pN/s. We note that the MD simulations suggest intermediate states (i.e., a well between these two barriers, sketched as a dashed blue line in the inset), which, however, cannot be extracted (or ruled out) by analyzing the force spectrum alone (33). Also, a third unbinding barrier further out at distances larger than 0.44 nm (indicated by the dashed red line in the inset) is seen in our experimental force curves and MD simulations and will be discussed below. However, in the force spectrum this barrier would only become kinetically dominant at lower loading rates than probed in our HS-FS experiments and is therefore not seen.

According to the Bell–Evans theory, one would expect two distinct slopes in the force spectrum, corresponding to the two kinetically relevant unbinding barriers (13). In our dynamic force spectrum, we observe, however, a rather continuous slope increase up to 10^{11} pN/s attributed to a force-induced shortening of the rupture length of these two barriers, as predicted by theories that take the shape of the barriers into account (14, 36). Finally, the slight deviation of the Brownian dynamics (BD) curve at very fast loading rates $>10^{11}$ pN/s may indicate a transition from a diffusion-dominated (Bell–Evans regime) to a deterministic regime (15, 34). For SA–b, this critical loading rate ($\dot{F}_c \gg F_c D x_\beta^{-2}$) $\sim 10^{11}$ pN/s (or $\sim 10^{10}$ nm/s) is orders of magnitude faster than that observed in previous HS-FS experiments of titin unfolding ($\sim 10^7$ pN/nm, $\sim 10^6$ nm/s) (24). This was expected since the transition is supposed to emerge when the pulling rate is faster than the intrinsic time required for the complex to explore its energy landscape. This intrinsic time was $(x_\beta^2/D) \sim 0.2 \text{ ms}$ for titin I91 but much shorter ($\sim 1 \text{ ns}$) for SA/b, which is reasonable given the less pronounced structural changes of the b molecule compared with partial titin domain unfolding.

The MD unbinding simulations (>300 in total) provided structural information on the loading-rate-dependent unbinding paths. Fig. 3A shows the distribution of center of mass (COM) distances from all MD trajectories between the SA binding pocket, defined as the set of amino acids that interact with the bound b in the static crystal structure, and the b molecule. The peak at 0 nm represents the bound state followed by two consecutive minima at $\sim 0.25 \text{ nm}$ and $\sim 0.5 \text{ nm}$. These values are

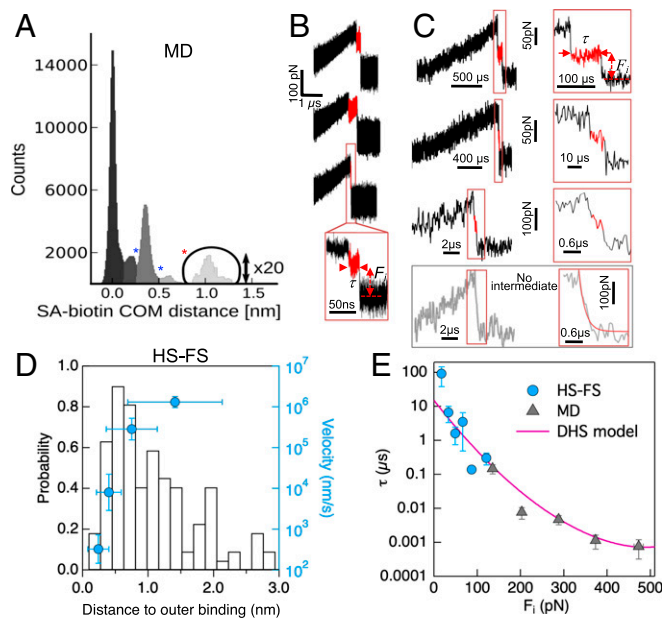


Fig. 3. Outer barrier. (A) Distribution of COM distances between SA and b for all MD trajectories during unbinding. The first two minima coincide with the barrier positions obtained from the Brownian dynamics simulations fit of the force spectrum in Fig. 2, Inset. (B) Examples of MD and (C, top three) HS-FS force–time curves showing outer binding. The lifetime and applied force of outer binding events was determined as shown (red lines) and described in Materials and Methods. The bottom curve shows an example for which no intermediate was observed. The red line shows an exponential fit with decay time $\sim 0.28 \mu\text{s}$. (D) Distribution of experimental distance to outer binding (left axis) and pulling velocity dependence of the average distance (blue, right axis). (E) Outer binding lifetime vs. applied force from HS-FS (circles) and MD simulations (triangles). The solid line shows the best fit to the force-dependent lifetime DHS model (14) with parameters $\tau_0 = 16 \pm 7 \mu\text{s}$, $x_\beta = 0.16 \pm 0.10 \text{ nm}$, and $\Delta G = 12 \pm 6 \text{ k}_B\text{T}$. This distance the outer barrier (x_β) should be added to the position of the second barrier at $x_{\beta 2} = 0.60 \text{ nm}$ in Fig. 2 (sketched as a dashed red line in the inset).

slightly left of the positions of the two barriers ($\sim 0.19 \text{ nm}$ and $\sim 0.44 \text{ nm}$) obtained from the BD fit of the force spectrum and suggest the COM distance as an appropriate reaction coordinate of unbinding. Interestingly, the peak between and to the right of these two minima suggests that, at least upon force application, one or several metastable states appear, as a result of the tilted energy landscape. Importantly, these metastable states will favor rebinding at sufficiently slow pulling rates (37, 38). The simulations show that most of the H-bonds between b and the SA binding pocket remain intact until b has moved $\sim 0.15 \text{ nm}$ toward the outside of the SA binding pocket. At the distance corresponding to the first barrier, the H-bonds between residues Ser27, Tyr43, Asn49, and Asp128 and the b, rather parallel to the pulling direction, rupture. Escape from the binding pocket occurs only after the second barrier at $\sim 0.5 \text{ nm}$, where most of the remaining H-bonds between b and SA (mainly with residues Asn49, Tyr54, and Arg84) rupture (Fig. 4B and SI Appendix, Fig. S9). Notably, these H-bonds are nearly perpendicular to the unbinding direction (long axis of the binding pocket), which implies a shear force, and only simultaneous failure of all H-bonds lead to dissociation, with subsequent transient formation of a different H-bond network (SI Appendix, Fig. S9). A similar mechanism has been observed before as key to providing stability against forced protein unfolding (39, 40). Overall, the geometry of rupture and reconfiguration of the H-bond network between b and adjacent amino acids of the binding pocket seems to represent the main determinants of the dynamic force spectrum in Fig. 2, described by the energy landscape with two barriers.

and small viscous damping were used: AC10 cantilevers with 600-kHz resonance frequency in liquid, 0.1 N/m spring constant, quality factor of 0.9, and $0.09 \text{ pN}\cdot\mu\text{m}^{-1}\cdot\text{s}^{-1}$ viscous coefficient; and shorter AC7 cantilevers, with 1.3-MHz resonance frequency in liquid, 0.6 N/m spring constant, quality factor of 0.6, and $0.05 \text{ pN}\cdot\mu\text{m}^{-1}\cdot\text{s}^{-1}$ viscous coefficient. The spring constant of the cantilevers was determined in air using the Sader method (46). The optical lever sensitivity was then determined in liquid from the thermal spectrum and the known spring constant (24, 47). Short HS-AFM cantilevers were placed on the cantilever holder immersed in the fluid cell with PBS buffer and placed on the HS-AFM. The SA agarose functionalized sample-stage was then mounted onto the fluid cell. Force curves were collected approaching the sample at a constant speed of $10 \mu\text{m/s}$ and indenting the SA agarose with the bylatted tip for 0.5 s at a constant force of $<500 \text{ pN}$. The sample was then retracted at varying retraction velocities from $0.010 \mu\text{m/s}$ to $30,000 \mu\text{m/s}$. Free b was titrated into the fluid cell to achieve a lower binding frequency of $\sim 5\%$ favoring single-bond interactions, ensuring that most of the events ($>95\%$) reported single-bond ruptures (48, 49). The reduction in binding frequency after adding free b further confirmed the specificity of the interaction. Representative examples of retraction force curves are shown in Fig. 1B. The sampling rate was set between 2 MS/s and 20 MS/s depending on the retraction speed of the experiment.

HS-FS Data Processing. Rupture events were detected using semiautomatic home-made routines (MATLAB; MathWorks) from the numerical derivative of the force curves by defining a threshold established by the zero-force baseline noise and depending on the sampling frequency and pulling rate (24). Force curves presenting rupture events were analyzed to measure the rupture forces, rupture lengths, and effective spring constant (Fig. 1B). Loading rates were determined from the slope before rupture (2 to 3 nm) of each force versus time trace. Rupture forces were pooled by loading rate and the corresponding histograms generated (SI Appendix, Figs. S1 and S2). Most probable rupture forces and SDs of rupture forces at each loading rate were calculated from Gaussian fits (SI Appendix, Figs. S1 and S2). When two peaks were clearly distinguishable in the force histograms, distributions were fitted using a bimodal function imposing the center of the second peak to be two times that of the first peak. Thus, the first center peak value was used as the average rupture force (SI Appendix, Figs. S1 and S2).

HS-FS Transient Binding. From the list of rupture events, transient or intermediate binding events were determined from the numerical derivative of the force drop region: from the main rupture event to the zero-force baseline (SI Appendix, Figs. S5 and S6). The numerical derivative of the force drop region was calculated by the five-point stencil method (50). An average filter with a window ranging from 0 to $25 \mu\text{s}$ was used according to pulling velocity and sampling rate. At the lowest velocities, due to the reduced sampling rate and the lower rupture forces, shortest events were likely missed. Transient binding events were defined from the time interval between the two most prominent minima within the force drop region including at least one data point of the force derivative with positive value. If this condition was not accomplished or the mean force value for the transient event was within one SD of the zero-force baseline, no rebinding event was considered. The lifetime of the intermediate state was determined from the time interval between these two minima. The force level was determined as the average force of the interval. The distance to the intermediate state (Fig. 3D) was calculated from the force versus extension curves as the distance from the extension at which the main rupture occurs to the average extension of the interval.

HS-FS Viscous Drag Correction. Viscous drag coefficients were calculated for each cantilever type from retraction curves by measuring the drag force exerted on the cantilever at various velocities near the substrate ($<200 \text{ nm}$) divided by the retraction velocity (51, 52). The cantilever coefficients on agarose beads were $0.09 \text{ pN}/(\mu\text{m}\cdot\text{s})$ and $0.05 \text{ pN}/(\mu\text{m}\cdot\text{s})$ for AC10 and AC7 cantilevers, respectively. The viscous drag was corrected by multiplying the viscous drag coefficient by the relative tip velocity. This correction was only significant ($\sim 8\%$ force correction) at the highest velocities achieved with each cantilever type.

MD Simulations. Force probe MD simulations were carried out using the Amber99sb (53) force field together with TIP3P (54) water model and virtual interaction sites (55). The electrostatic interaction was calculated with particle-mesh Ewald (56) with a real space cutoff of 1 nm, a grid spacing of 0.12 nm, and cubic interpolation. The same cutoff length was used for the van der Waals interaction. All atom bonds were constraint using LINCS algorithm (57). All simulations were performed at a constant number of

particles and a constant temperature coupled to a heat bath at 300 K using the velocity rescaling method (58) and a coupling constant of 0.2 ps. We used the Verlet algorithm (59) with a time step of 4 fs to integrate the equation of motion. In the experimental setup, the cantilever, here described by a harmonic potential with a spring constant $k_{\text{pull}} = 100 \text{ pN/nm}$, was attached to b via a PEG linker. The harmonic potential was moved away from the binding pocket at 12 different velocities, ranging from 0.001 m/s up to 50 m/s . Depending on the applied loading rate the center of the harmonic pulling potential moved up to 12 nm until the simulation was stopped, ensuring that b is completely unbound from SA. In the simulations the linker was described by a WLC potential,

$$U_{\text{wlc}}(x) = \frac{k_B T l_c}{4 l_p} \left(1 - \frac{x + x_{\text{start}}}{l_c} \right)^{-1} - \frac{k_B T (x + x_{\text{start}})}{4 l_p} + \frac{k_B T (x + x_{\text{start}})^2}{2 l_c l_p},$$

with a persistence length $l_p = 1.4 \text{ nm}$ and a contour length $l_c = 10 \text{ nm}$, similar to the experimental values (Fig. 1, simulation setup), which was added to GROMACS as a tabulated bonded potential (54). To keep the simulation box size small we shifted the WLC potential by a constant $x_{\text{start}} = 7 \text{ nm}$, nevertheless making sure that the forces required to stretch the linker were lower than those to rupture the complex. All simulations were performed at a sodium chloride concentration of 150 mM. The simulation box sizes perpendicular to the pulling direction were chosen to be 8.5 nm, which is a minimal distance of 0.7 nm between the solute and the periodic boundaries, leading to a minimum distance between SA and its periodic image of more than 1.4 nm. The box length in the pulling direction varied between 18 nm for the faster and 13 nm for the slowest simulations.

The starting structure for the simulations was based on the tetramer PDB ID code 3RY2 (4). In case of the tetramer, only one b was pulled out of the binding pocket to ensure single unbinding events.

Rupture forces and loading rates were determined for each individual force curve. As for experiments, the loading rate was also determined from the slope of the force–time curve before rupture. We calculated the mean and SD of the rupture forces for each loading rate.

Brownian Dynamics Simulations. To extract information on the underlying free-energy landscape along the unbinding reaction coordinate, and in addition to the application of the simple Bell model and more sophisticated theoretical approaches [BSK (15), Friddle–Noy–deYoreo (FNdy) (37), Dudko–Hummer–Szabo (DHS) (14), and CHS (36)], numerical simulations of enforced unbinding with one-dimensional energy landscapes were carried out. To that end, the Smoluchowski equation,

$$\partial_t \rho(x, t) = \nabla D [\nabla - \beta(\nabla V(x, t))] \rho(x, t),$$

was solved numerically for a time-dependent potential $V(x, t) = V_0(x) - \dot{F}xt$, where $\beta = 1/k_B T$ and \dot{F} is the applied loading rate. As underlying unbinding potential, a double-barrier potential $V_0(x) = 2\Delta G_1(x)^2(1.5 - y(x))$ for $x \leq x_{p1}$ was chosen, with barrier height ΔG_1 of the first barrier. The function $y(x) = \left((c_1 \frac{x}{x_{p1}} + c_2) \frac{x}{x_{p1}} + \omega_1 \right) \frac{x}{x_{p1}}$, with the constants $c_1 = \omega_1 + \omega_2 - 2$ and $c_2 = 3 - 2\omega_1 - \omega_2$, served to control the shape of the first barrier, particularly the curvatures ω_1 and ω_2 of the well and, respectively, that at the first barrier top. The above function also serves to control the rupture length x_{p1} , here defined as the distance between first barrier top and minimum of the well of the bound state.

For $x_{p1} < x < x_{p2}$ the potential becomes

$$V_{x > x_{p1}}(x) = V_0(x_{p1}) + 2(\Delta G_2 - \Delta G_1)y(x)^2(1.5 - y(x))$$

with $y(x) = \frac{x - x_{p1}}{x_{p2} - x_{p1}}$ and the position of the second barrier x_{p2} . For all $x > x_{p2}$ the potential is set to ΔG_2 , the height of the second barrier.

Trajectories were generated starting from a Boltzmann ensemble $\rho_0(x)/\exp(V_0(x))$ within the well of the bound state. Positions were updated to first order according to the solution of the Smoluchowski equation for linear potential,

$$x_{\text{new}} := x_{\text{old}} - \frac{D\Delta t}{k_B T} \nabla V(x, t) + \frac{1}{\sqrt{2D\Delta t}} \xi(t),$$

with an integration time step of 0.5 ps, which ensured that less than 5% of the integration steps were larger than $0.05 x_{p1}$. A Gaussian distributed (variance one) random force $\xi(t)$ was used. A diffusion constant $D = k_B T / \gamma = 4 \cdot 10^{-11} \text{ m}^2/\text{s}$ was found to provide the best fit to the force spectrum.

To reduce computational effort and thus to facilitate the generation of trajectories even for the slowest loading rates, an appropriate biasing potential

$$V_{\text{bias}}(x, t) = a \left(\frac{x}{x_{\beta}} \right)^n + v(t)$$

was added whenever the (actual) barrier height exceeded 5 $k_B T$, with

$$a = \frac{1}{nc^{n-1}}, \quad c = \frac{nv}{n-1}$$

and v adapted such that the barrier height of the resulting total potential $V(x, t) + V_{\text{bias}}(x, t)$ remained between 5 and 7 $k_B T$ at all times. To compensate for the reduced barrier height due to the biasing potential and the increased barrier transition probability per integration step, the integration step size was dynamically rescaled by an acceleration factor $Z_{\text{bias}}(t) = Z_0(t)$, where Z_0 and Z_{bias} are the partition functions of the unperturbed and, respectively, perturbed bound states:

$$Z_0(t) = \int_{-\infty}^{x_b} \exp(-\beta V(x, t)) dx$$

and

$$Z_{\text{bias}}(t) = \int_{-\infty}^{x_b} \exp(-\beta(V(x, t) + V_{\text{bias}}(x, t))) dx.$$

For each of the loading rates for which experimental or MD simulation derived rupture forces were obtained (Fig. 2), 1,000 trajectories were generated and the resulting individual force at the point of barrier crossing were averaged. The fitting parameters ΔG_1 , ΔG_2 , $x_{\beta 1}$, $x_{\beta 2}$, ω_1 , and ω_2 were varied using simple line-scanning until the χ^2 (weighted by the SEM) relative to the 37 experimental/simulation averaged rupture forces was minimal. Uncertainties of the six fitting parameters (given in the caption of *SI Appendix, Fig. S7*) were estimated conservatively via nonparametric bootstrapping with 80 replica datasets, each of which was generated by randomly drawing 37 from the 37 rupture forces (allowing for multiple draws of the same data point). Parametric bootstrapping using a Gaussian error model and the SEMs rupture forces yielded slightly smaller uncertainties.

COM Distributions. To calculate the distributions of the COM distance of each MD trajectory, we calculated the distance between the COM of the binding-pocket-forming residues (L25, S27, Y43, S45, V47, G48, A50, W79, R84, A86,

S88, T90, W92, W108, L110, and D128) and the COM of b. This was done starting shortly before rupture and ending when the distance between b and the binding pocket was larger 4 nm.

As we do not see any binding patterns further away than 2 nm we reduced the plotted histograms to a maximal distance of 2 nm. The COM distances were then binned into 200 equally spaced bins and normalized by the total amount of data points.

MD Intermediate States and Transition Plots. To determine the intermediate states, we split the COM distance distributions according to the dominant peaks, such that each peak represents a different intermediate state. We then calculated the transition rates by counting the transitions from state s_i to state s_j and subtracted the amount of back-transitions (s_j to s_i) for each combination, resulting in a net transition of -1 , 0 , or 1 . Finally, each rate was averaged for each velocity.

The probabilities for being in an intermediate state were calculated by counting the total time that an intermediate state is visited normalized by the total time spent in all intermediate states. The time spent in the ground state and the unbound state were not taken into account to provide comparability, as the time spent in either of them is arbitrary and depends only on the chosen starting and end point of the rupture event.

Principal Component Analysis of Loop 3–4. To understand the different unbinding pathways, we analyzed the motion of loop 3–4 by performing a principal component analysis on the backbone atoms of residues 44–54. Therefore, a representative simulation was used to calculate the characteristic eigenvectors of the loop 3–4 motion going from a closed conformation (negative values) to an open conformation (positive values). All other simulations were projected onto the first eigenvector and analyzed depending on the applied loading rate regime. The time-resolved projections were finally binned along the COM distance and the average projection on the first eigenvector for each loading rate regime was calculated (*SI Appendix, Fig. S10*).

ACKNOWLEDGMENTS. F.R. and H.G. thank Prof. Klaus Schulten for inspiring discussions, and F.R. and S.S. thank Prof. Toshio Ando for generously providing AC7 cantilevers. This work was supported in part by the Agence Nationale de la Recherche Grants ANR-15-CE11-0007 (BioHSFS) and ANR-11-LABX-0054 (Labex INFORM), European Cooperation in Science & Technology Action TD1002-10006, and Deutsche Forschungsgemeinschaft Grant SFB 755.A5.

- Koshland DE (1958) Application of a theory of enzyme specificity to protein synthesis. *Proc Natl Acad Sci USA* 44:98–104.
- Fischer E (1894) Einfluss der configuration auf die wirkung der enzyme. *Ber Dtsch Chem Ges* 27:2985–2993.
- Frederick KK, Marlow MS, Valentine KG, Wand AJ (2007) Conformational entropy in molecular recognition by proteins. *Nature* 448:325–329.
- Le Trong I, et al. (2011) Streptavidin and its biotin complex at atomic resolution. *Acta Crystallogr D Biol Crystallogr* 67:813–821.
- Chilkoti A, Stayton PS (1995) Molecular-origins of the slow streptavidin-biotin dissociation kinetics. *J Am Chem Soc* 117:10622–10628.
- Laitinen OH, Hytönen VP, Nordlund HR, Kulomaa MS (2006) Genetically engineered avidins and streptavidins. *Cell Mol Life Sci* 63:2992–3017.
- Hyre DE, et al. (2006) Cooperative hydrogen bond interactions in the streptavidin-biotin system. *Protein Sci* 15:459–467.
- Koussa MA, Halvorsen K, Ward A, Wong WP (2015) DNA nanoswitches: A quantitative platform for gel-based biomolecular interaction analysis. *Nat Methods* 12:123–126.
- Chivers CE, et al. (2010) A streptavidin variant with slower biotin dissociation and increased mechanostability. *Nat Methods* 7:391–393.
- Merkel R, Nassoy P, Leung A, Ritchie K, Evans E (1999) Energy landscapes of receptor-ligand bonds explored with dynamic force spectroscopy. *Nature* 397:50–53.
- Florin EL, Moy VT, Gaub HE (1994) Adhesion forces between individual ligand-receptor pairs. *Science* 264:415–417.
- Lee GU, Kidwell DA, Colton RJ (1994) Sensing discrete streptavidin biotin interactions with atomic-force microscopy. *Langmuir* 10:354–357.
- Evans E, Ritchie K (1997) Dynamic strength of molecular adhesion bonds. *Biophys J* 72:1541–1555.
- Dudko OK, Hummer G, Szabo A (2006) Intrinsic rates and activation free energies from single-molecule pulling experiments. *Phys Rev Lett* 96:108101.
- Bullerjahn JT, Sturm S, Kroy K (2014) Theory of rapid force spectroscopy. *Nat Commun* 5:4463.
- Teulon J-M, et al. (2011) Single and multiple bonds in (strept)avidin-biotin interactions. *J Mol Recognit* 24:490–502.
- Moy VT, Florin EL, Gaub HE (1994) Intermolecular forces and energies between ligands and receptors. *Science* 266:257–259.
- Sedlak SM, et al. (2017) Monodisperse measurement of the biotin-streptavidin interaction strength in a well-defined pulling geometry. *PLoS One* 12:e0188722.
- Rico F, Moy VT (2007) Energy landscape roughness of the streptavidin-biotin interaction. *J Mol Recognit* 20:495–501.
- Jeny S, Mor F, Koszali R, Forró L, Moy VT (2010) Monitoring ligand-receptor interactions by photonic force microscopy. *Nanotechnology* 21:255102.
- Pincet F, Husson J (2005) The solution to the streptavidin-biotin paradox: The influence of history on the strength of single molecular bonds. *Biophys J* 89:4374–4381.
- Neupane K, et al. (2016) Direct observation of transition paths during the folding of proteins and nucleic acids. *Science* 352:239–242.
- Yu H, Siewny MGW, Edwards DT, Sanders AW, Perkins TT (2017) Hidden dynamics in the unfolding of individual bacteriorhodopsin proteins. *Science* 355:945–950.
- Rico F, Gonzalez L, Casuso I, Puig-Vidal M, Scheuring S (2013) High-speed force spectroscopy unfolds titin at the velocity of molecular dynamics simulations. *Science* 342:741–743.
- Takahashi H, Rico F, Chipot C, Scheuring S (2018) α -Helix unwinding as force buffer in spectrins. *ACS Nano* 12:2719–2727.
- Grubmüller H, Heymann B, Tavan P (1996) Ligand binding: Molecular mechanics calculation of the streptavidin-biotin rupture force. *Science* 271:997–999.
- Izrailev S, Stepaniants S, Balsera M, Oono Y, Schulten K (1997) Molecular dynamics study of unbinding of the avidin-biotin complex. *Biophys J* 72:1568–1581.
- Walton EB, Lee S, Van Vliet KJ (2008) Extending Bell's model: How force transducer stiffness alters measured unbinding forces and kinetics of molecular complexes. *Biophys J* 94:2621–2630.
- Yuan C, Chen A, Kolb P, Moy VT (2000) Energy landscape of streptavidin-biotin complexes measured by atomic force microscopy. *Biochemistry* 39:10219–10223.
- Abraham MJ, et al. (2015) GROMACS: High performance molecular simulations through multi-level parallelism from laptops to supercomputers. *SoftwareX* 1:19–25.
- Kutzner C, et al. (2015) Best bang for your buck: GPU nodes for GROMACS biomolecular simulations. *J Comput Chem* 36:1990–2008.
- Hinterdorfer P, Baumgartner W, Gruber HJ, Schilcher K, Schindler H (1996) Detection and localization of individual antibody-antigen recognition events by atomic force microscopy. *Proc Natl Acad Sci USA* 93:3477–3481.
- Heymann B, Grubmüller H (2000) Dynamic force spectroscopy of molecular adhesion bonds. *Phys Rev Lett* 84:6126–6129.
- Hummer G, Szabo A (2003) Kinetics from nonequilibrium single-molecule pulling experiments. *Biophys J* 85:5–15.
- Makarov DE (2014) Communication: Does force spectroscopy of biomolecules probe their intrinsic dynamic properties? *J Chem Phys* 141:241103.
- Cossio P, Hummer G, Szabo A (2016) Kinetic ductility and force-spike resistance of proteins from single-molecule force spectroscopy. *Biophys J* 111:832–840.

37. Friddle RW, Noy A, De Yoreo JJ (2012) Interpreting the widespread nonlinear force spectra of intermolecular bonds. *Proc Natl Acad Sci USA* 109:13573–13578.
38. Dudko OK (2016) Decoding the mechanical fingerprints of biomolecules. *Q Rev Biophys* 49:e3.
39. Lu H, Schulten K (2000) The key event in force-induced unfolding of Titin's immunoglobulin domains. *Biophys J* 79:51–65.
40. Gräter F, Shen J, Jiang H, Gautel M, Grubmüller H (2005) Mechanically induced titin kinase activation studied by force-probe molecular dynamics simulations. *Biophys J* 88:790–804.
41. Wolynes PG (1997) Folding funnels and energy landscapes of larger proteins within the capillarity approximation. *Proc Natl Acad Sci USA* 94:6170–6175.
42. Voß B, Seifert R, Kaupp UB, Grubmüller H (2016) A quantitative model for camp binding to the binding domain of mlok1. *Biophys J* 111:1668–1678.
43. Wang J, Verkhivker GM (2003) Energy landscape theory, funnels, specificity, and optimal criterion of biomolecular binding. *Phys Rev Lett* 90:188101.
44. Hohsaka T, et al. (2004) Position-specific incorporation of dansylated non-natural amino acids into streptavidin by using a four-base codon. *FEBS Lett* 560:173–177.
45. Murakami H, Hohsaka T, Ashizuka Y, Hashimoto K, Sisido M (2000) Site-directed incorporation of fluorescent nonnatural amino acids into streptavidin for highly sensitive detection of biotin. *Biomacromolecules* 1:118–125.
46. Sader JE, et al. (2016) A virtual instrument to standardise the calibration of atomic force microscope cantilevers. *Rev Sci Instrum* 87:093711.
47. Sumbul F, Marchesi A, Takahashi H, Scheuring S, Rico F (2018) High-speed force spectroscopy for single protein unfolding. *Nanoscale Imaging: Methods and Protocols*, ed Lyubchenko YL (Springer, New York), pp 243–264.
48. Tees DFJ, Waugh RE, Hammer DA (2001) A microcantilever device to assess the effect of force on the lifetime of selectin-carbohydrate bonds. *Biophys J* 80:668–682.
49. Johnson KC, Thomas WE (2018) How do we know when single-molecule force spectroscopy really tests single bonds? *Biophys J* 114:2032–2039.
50. Sauer T (2011) *Numerical Analysis* (Pearson, Essex, UK).
51. Janovjak H, Struckmeier J, Müller DJ (2005) Hydrodynamic effects in fast AFM single-molecule force measurements. *Eur Biophys J* 34:91–96.
52. Alcaraz J, et al. (2002) Correction of microrheological measurements of soft samples with atomic force microscopy for the hydrodynamic drag on the cantilever. *Langmuir* 18:716–721.
53. Hornak V, et al. (2006) Comparison of multiple Amber force fields and development of improved protein backbone parameters. *Proteins* 65:712–725.
54. Jorgensen WL, Chandrasekhar J, Madura JD, Impey RW, Klein ML (1983) Comparison of simple potential functions for simulating liquid water. *J Chem Phys* 79:926–935.
55. Feenstra KA, Hess B, Berendsen HJC (1999) Improving efficiency of large time-scale molecular dynamics simulations of hydrogen-rich systems. *J Comput Chem* 20:786–798.
56. Darden T, York D, Pedersen L (1993) Particle mesh Ewald: An $N\log(N)$ method for Ewald sums in large systems. *J Chem Phys* 98:10089–10092.
57. Hess B, Bekker H, Berendsen HJC, Fraaije JGEM (1997) LINCS: A linear constraint solver for molecular simulations. *J Comput Chem* 18:1463–1472.
58. Bussi G, Donadio D, Parrinello M (2007) Canonical sampling through velocity rescaling. *J Chem Phys* 126:014101.
59. Verlet L (1967) Computer “experiments” on classical fluids. I. Thermodynamical properties of Lennard-Jones molecules. *Phys Rev* 159:98–103.